Wear ∎ (∎∎∎∎) ∎∎∎–∎∎∎

Contents lists available at ScienceDirect

Wear

journal homepage: www.elsevier.com/locate/wear

Evaluation of cavitation-induced pressure loads applied to material surfaces by finite-element-assisted pit analysis and numerical investigation of the elasto-plastic deformation of metallic materials

F. Pöhl [a,*], S. Mottyll [b], R. Skoda [b], S. Huth [a]

[a] Ruhr-Universität Bochum, Chair of Materials Technology, 44780 Bochum, Germany
[b] Ruhr-Universität Bochum, Chair of Hydraulic Fluid Machinery, 44780 Bochum, Germany

ARTICLE INFO

Article history:
Received 1 September 2014
Received in revised form
26 December 2014
Accepted 27 December 2014

Keywords:
Cavitation
Pressure load
Pit analysis
CFD

ABSTRACT

Implosion of cavitation bubbles close to a material applies a high pressure load on the surface that leads to cyclic, elasto-plastic deformation followed by damage and loss of material. The load strongly depends on the flow conditions and its experimental determination is extremely difficult. This study presents a method for quantitative calculation of the pressure loads induced by collapsing bubbles. This method is based on the analysis of pits on the material surface formed within the incubation period. The pits are footprints of collapsing bubbles and are measured by atomic force microscopy (AFM). An inverse algorithm based on finite element method (FEM) simulations is then used to determine the pressure load that is necessary to form the measured pits. The pressure fields, which are assumed to be axially symmetric (bell-shape profile), were calculated for cavitation pits formed in pure copper. The pits were induced by short-term exposure to cavitation in an ultrasonic cavitation testing device. Additionally, the elasto-plastic deformation of copper was numerically (FEM) investigated for a given cavitation load. It was found that the deformation is mostly elastic and that the maximum stress is located in a subsurface region. The maximum pressure of the cavitation load, the resulting maximum plastic strain in the material, and the ratio of the elastic to total deformation work correlate well with the ratio of pit width to pit depth. In order to evaluate the simplified assumption of a static pressure profile (bell-shape), the calculated pressure loads were critically compared to those determined by a detailed single bubble simulation with a compressible CFD flow algorithm. The maximum pressure profiles of the highly-transient CFD results show partly significant deviations dependent on the non-dimensional bubble stand-off distance to the wall. An improved pressure load profile and transient effects will be considered next in the FEM algorithm.

1. Introduction

Cavitation in hydraulic fluid machinery such as pipes, valves, ship propellers, pumps, and turbines leads to wear of their components (cavitation erosion). Consequences of cavitation erosion include negative effects such as failure of components, reduction in efficiency, noise, or vibration [1]. Cavitation erosion is attributed to the collapse of individual cavitation bubbles in the vicinity of the material's surface [2]. Repeated collapses apply local cyclic pressure loads to the surface, which lead to damage and loss of material [3]. Quantitative knowledge of the induced pressure loads is crucial for understanding the material behavior and the underlying deformation processes. Thus, a precise understanding of cavitation erosion of materials implies a detailed knowledge of both the material behavior and the applied load.

Much research has been focused on the deformation processes of materials under cavitation load [4–10]. However, it is difficult to obtain detailed and quantitative knowledge of the load induced by cavitation due to the extremely small scales of duration and localization on the surface. One possible method of measuring the impact pressure is to use pressure sensors such as piezoelectric films [11]. However, these sensors do not generally provide an accurate measurement under the present conditions [12,13]. Another method of estimating the pressure load is the analysis of pits formed on the material surface within the incubation period. The pits are the footprints of collapsing bubbles and are formed due to the high local pressure by plastic deformation. Tzanakis et al. investigated pits caused by collapsing bubbles in an

* Corresponding author.
E-mail address: poehl@wtech.rub.de (F. Pöhl).

http://dx.doi.org/10.1016/j.wear.2014.12.048
0043-1648/

ultrasonic test device and estimated the corresponding pressures with the analogy of spherical indentation [12]. They determined impact pressures in the range of approx. 400–1400 MPa. Carnelli et al. analyzed cavitation pits caused by a cavitation field in a hydrodynamic tunnel [13]. Using the analogy of spherical indentation and instrumented indentation testing, they determined peak loads of hydrodynamic pressures to be approx. 1000–1600 MPa. Lauer et al. used numerical simulations to calculate single bubble collapse events leading to pressure loads on the material surface of up to approx. 6000 MPa [14].

These different estimates show that the load strongly depends on the flow conditions. Thus, results cannot be transferred to different fluid machineries or test devices. For these reasons, the cavitation-induced loads on materials are not known for most fluid machineries or cavitation erosion test devices.

The resistance to cavitation erosion is often tested in ASTM G32 standardized vibratory apparatus (ultrasonic transducer) [15]. In spite of, being a standardized test, the local pressure loads caused by collapsing bubbles are not known. This paper presents a method for the quantitative calculation of the pressure loads induced by collapsing bubbles. The method is applied to cavitation pits formed in the standardized ultrasonic vibratory apparatus. In analogy to the approach of Tzanakis et al. and Carnelli et al., the method is based on the analysis of cavitation pits that form within the incubation period [12,13]. However, a FEM-based inverse algorithm is used to calculate the pressure field that is necessary to form a given pit, taking into account the local strength of the material. In addition, FEM simulations give an insight into the deformation processes of the material and create a link between load and deformation.

In this study, single, non-overlapping cavitation pits are analyzed in order to calculate the corresponding pressure that is necessary to form the pits. However, it is also known that cavitation clouds occur and the resulting pressure loads might be higher and more complex compared to single collapsing bubbles [16]. In addition, attention must be paid to the influence of strain rate or temperature, which are not taken into account. The extremely rapid bubble collapse and high deformation speed as well as an increase in temperature may influence the deformation behavior [17,18]. The pressure field in the FEM model is assumed to be axially symmetric with a pressure maximum located at the axis of symmetry and calculated for this ideal shape (see Section 2.5). Due to these assumptions the pressures determined by the inverse algorithm based on pit analysis are compared to the load profiles calculated from CFD simulations of near-wall vapor bubble collapses. The CFD simulations are also used to try a first reconstruction of possible bubble collapse scenarios that lead to the pressure calculated with the FEM-based algorithm.

This paper addresses following issues:

- Determination of the pressure applied locally to material surfaces by collapsing cavitation bubbles in the standardized ultrasonic vibratory apparatus. The pressure loads, which are assumed to follow an idealized axially symmetric shape, are reconstructed with a numerical (FEM) inverse algorithm based on the pit analysis. Due to the assumptions made within the inverse algorithm wall pressures are additionally calculated with single bubble CFD simulations.
- Numerical analysis (FEM) of the elasto-plastic deformation processes of pure copper under the calculated pressure loads with the FEM-based inverse algorithm.
- Relating the measured pit geometries, calculated pressures, and material deformation to each other.
- Comparing pressures calculated from the pit geometry to those determined by the detailed CFD single bubble simulation and reconstruction of possible bubble collapse scenarios.

2. Material and methods

The experimental and numerical procedures for calculating the cavitation-induced pressure loads based on measured pit geometries are summarized in Fig. 1. The key element is an inverse algorithm that compares a measured to a numerically calculated pit geometry. The numerical pit geometry is calculated with a finite-element-method (FEM) model with an assumed pressure distribution $p(x)$ acting on the surface. The pressure field $p(x)$ is subsequently adjusted until the numerically calculated pit geometry fits to an experimentally measured one. This is achieved by minimizing the error between the numerical and the experimental

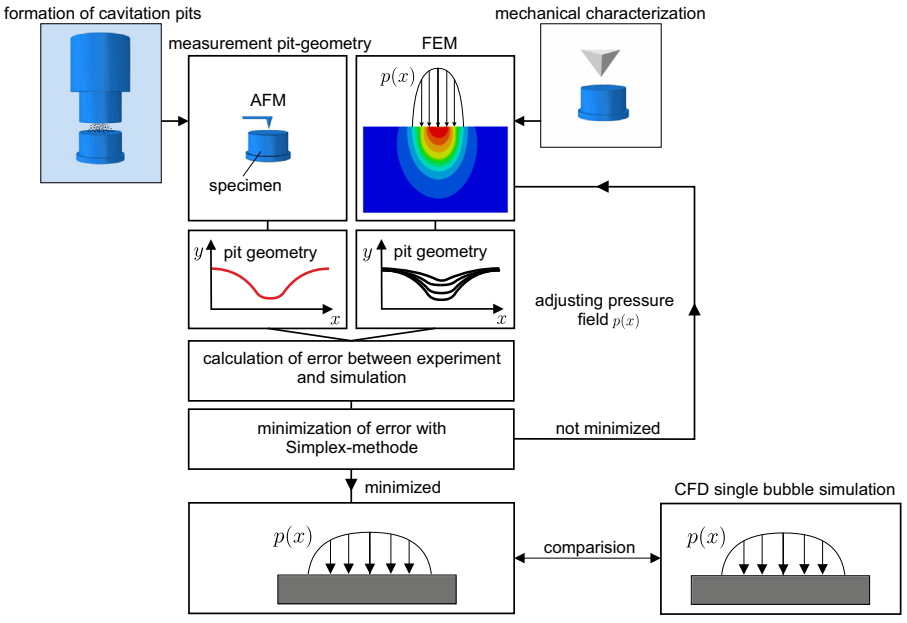

Fig. 1. Schematic illustration of the numerical and experimental procedures to calculate the cavitation-induced pressure loads on material surfaces based on measured pit geometries.

Please cite this article as: F. Pöhl, et al., Evaluation of cavitation-induced pressure loads applied to material surfaces by finite-element-assisted pit analysis and numerical investigation of the..., Wear (2015), http://dx.doi.org/10.1016/j.wear.2014.12.048

pit geometries. The algorithm needs two sets of experimental input data: the mechanical behavior of the investigated material and the geometry of the cavitation pits.

The mechanical properties of the investigated material were determined by instrumented indentation testing. An inverse method described in [19] was applied to the results of the indentation tests to determine the local uniaxial stress–strain behavior, which is the necessary input data for the numerical calculations. Short-term cavitation tests were conducted in the ASTM G32 standardized ultrasonic vibratory apparatus described in [5] to generate single cavitation pits. The geometries of the induced pits were measured with an atomic force microscope (AFM). Knowledge of the mechanical properties and pit geometries enabled calculation of the pressure loads. FEM simulations were employed to simulate elasto-plastic deformation of the material for given mechanical behavior and loads. Additionally, the calculated pressure loads were compared to those determined by a detailed CFD single bubble simulation.

2.1. Material

In order to generate single pits on the surface, pure polycrystalline copper (99.99%) was investigated. Owing to its low strength, single cavitation pits are easily formed on the surface during short-time exposure to cavitation. Prior to mechanical characterization and exposure to cavitation, the specimen was mechanically ground with SiC paper and polished with diamond suspensions having average grain sizes of 6, 3, and 1 μm, respectively. Fig. 2 shows the polycrystalline microstructure after etching at ambient temperature with a solution consisting of 100 ml distilled water and 10 g ammonium persulfate.

2.2. Instrumented indentation testing

The mechanical properties are necessary input data for the algorithm that calculates the impact pressure caused by collapsing cavitation bubbles. The uniaxial stress–strain behavior of the material is required for the numerical calculations within the algorithm. The load–displacement curves of Berkovich and cube corner indenters provide the parameters for the inverse determination of the uniaxial stress–strain curve. The underlying approach of the inverse method is based on an energy-based analysis of the indentation problem given in [20]. The analysis was used to derive relationships between the parameters of the load–displacement curve (e.g. loading curvature C) and the material parameters of the Ludwik power-law.

In order to measure the load–displacement curves instrumented indentation tests were conducted on a CSM NHT indenter equipped with a Berkovich and cube corner diamond tip. The maximum indentation depth was 4 μm with a loading and unloading rate of 2 μm/min and a dwell time of 10 s at maximum load. At least ten measurements were performed for each indenter geometry. The hardness and Young's modulus were calculated with the Oliver and Pharr method [21,22]. On the basis of measured load–displacement curves, the inverse procedure, described in [19], was used to determine the stress–strain behavior of the material.

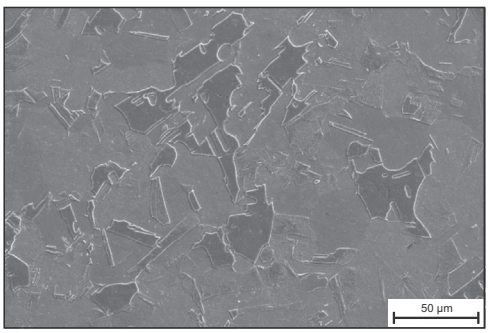

Fig. 2. Scanning electron microscope image of the polycrystalline microstructure of the investigated copper specimen.

It has been established that metallic materials can show an increase in strength with decreasing indentation depth [23]. This phenomenon is caused by surface hardening due to mechanical sample preparation, and in the case of self-similar indenters (Berkovich and cube corner), additionally superimposed by the well-known indentation size effect (ISE) [24,25]. Cavitation pits show a geometrical analogy to indentation imprints. Furthermore, the investigated pits on the copper specimen have depths in the range of a few hundred nm, where the nanoindentation data of copper show an intense size effect [26]. This implies that a similar size effect should be present during cavitation loading. As a consequence, the local strength of the material will not be the macroscopically observed and possible size effects need to be accounted for. It was thus assumed that a similar size effect is present, and the mechanical uniaxial stress–strain behavior was derived on the basis of the ISE-affected measured load–displacement curves.

2.3. Ultrasonic vibratory apparatus

The exposure time to cavitation in the ASTM G32 standardized ultrasonic cavitation testing device was 10 s. This time was sufficient to generate a large number of isolated, non-overlapping pits on the copper sample. The tests were performed with an amplitude of 40 μm and, a frequency of 30 kHz in distilled water at ambient temperature.

2.4. Atomic force microscopy

The geometry of induced pits was measured with an atomic force microscope (Bruker type nanos) in the contact mode. The scanning speed was 25 μm/s. Evaluation and analysis of the recorded images was conducted with Image Plus software (version 2.19).

2.5. Inverse algorithm for calculating the impact pressure from measured pit geometries

The inverse algorithm for calculating the cavitation-induced pressure is schematically illustrated in Fig. 1. The experimental input data are the material behavior of the copper specimen and the pit geometry measured by atomic force microscopy. The fundamental element of the algorithm is an FEM model. For given material parameters of the copper specimen, the model numerically calculates the pit geometry for an assumed pressure distribution $p(x)$ on the material surface. In the next step, the numerical pit geometry is compared to the experimental geometry and the error between the two is calculated. The error is then minimized by adjusting the pressure field until an agreement between the numerically and experimentally determined pit geometries is achieved using a minimization process based on the Simplex method [27].

Since most of the not-overlapping cavitation pits found on the copper specimen are nearly axially symmetric, the pressure field acting on the material surface is assumed to be also axially symmetric and given by Eq. (1). The pressure field is schematically illustrated in Fig. 3. The parameters σ_{max}, σ_b and α control the height, width, and the curvature of the field, respectively. For a given pit radius a, two of the three parameters (σ_{max}, σ_b and α) are adjusted in the algorithms to achieve an agreement between the

Please cite this article as: F. Pöhl, et al., Evaluation of cavitation-induced pressure loads applied to material surfaces by finite-element-assisted pit analysis and numerical investigation of the..., Wear (2015), http://dx.doi.org/10.1016/j.wear.2014.12.048

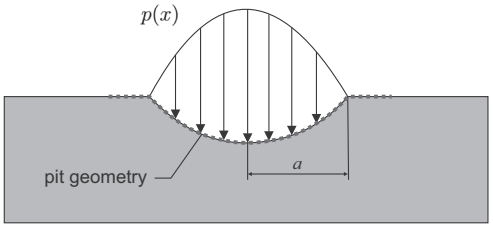

Fig. 3. Schematic illustration of an axially symmetric cavitation pit and the assumed pressure field $p(x)$ on the surface.

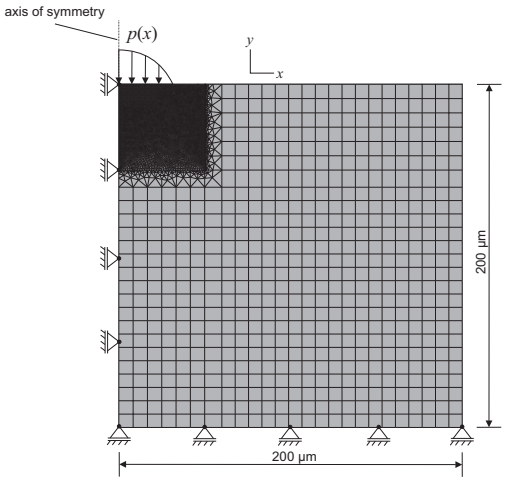

Fig. 4. Mesh, geometry and boundary conditions of the FEM model.

numerically and experimentally determined pit geometries:

$$p(x) = \sigma_{max} - \alpha(\sigma_b \cdot x)^2 \quad (1)$$

FEM calculations were performed using the FE software ABAQUS (version 6.11). The axisymmetric 2D model, including the geometry, mesh, and boundary conditions, is based on prior work and is shown in Fig. 4 [20,28]. The pressure field $p(x)$ given by Eq. (1) is applied to the material surface. The domain has dimensions of 200 $\times$ 200 µm. The modeled sample is restricted by symmetry boundary conditions along the axis of symmetry and by floating supports along the lower edge. The area in close proximity to the pressure field is meshed finely using CAX4R (four-node axisymmetric element) elements with reduced integration and hourglass control. To minimize the calculation effort, the fine mesh at the pressure field is migrated to a coarse mesh, which also consists of CAX4R elements. The transition region between the fine and coarse meshes consists of CAX3 (three-node axisymmetric element) elements. The total number of elements is approximately 10,000, depending on the measured pit geometry. The mesh of the model was adjusted to the pit geometry in such a way that the mesh quality remains constant and ensures accurate results.

The elastic material behavior of the copper specimen was modeled with Young's modulus $E = 130$ GPa and Poisson's ratio $\nu = 0.35$. The J_2 von Mises flow theory was used to model plasticity. The elasto-plastic material behavior is assumed to follow the Ludwik power law (Eq. (2)) with isotropic hardening and is described by three independent parameters: strength coefficient K, strain hardening exponent n, and Young's modulus E. The yield stress σ_y is then a depending variable and is given by Eq. (3) [29]. The parameters determined with instrumented indentation testing and inverse analysis are shown in Fig. 5. The assumed depth dependency of the material parameters is explained in Section 3. Strain rate and temperature effects are neglected. The FEM model was used to calculate the pressure load induced by collapsing bubbles

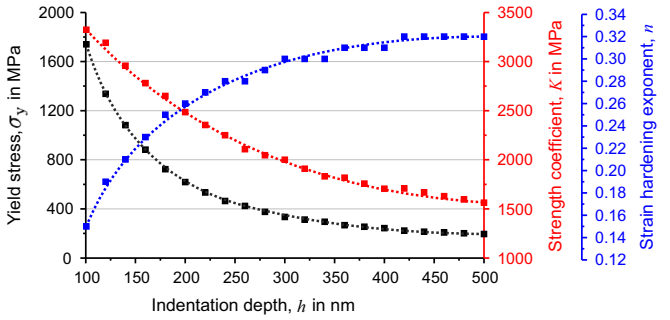

Fig. 5. Depth-dependent (size effects) material parameters of copper determined by instrumented indentation testing and inverse analysis.

within the algorithm and to investigate the elasto-plastic deformation of copper under the determined pressures:

$$\sigma = \begin{cases} E \cdot \varepsilon, & \sigma \le \sigma_y \\ K \cdot \varepsilon^n, & \sigma \ge \sigma_y \end{cases} \quad (2)$$

$$\sigma_y = \left(\frac{E^n}{K}\right)^{1/(n-1)} \quad (3)$$

2.6. CFD method

Bubbles collapsing in the vicinity of the wall generate high pressure pulses and shock waves [30] which can form high-speed re-entrant jets that strike the nearby wall with water-hammer-like impact pressures [31]. This phenomenon has been studied numerically by many authors, e.g. Lauer et al. [14], who used a compressible flow solver with a non-equilibrium thermodynamic model and a level set method in order to analyze collapse evolution and jet formation under high ambient-pressure conditions. Johnsen and Colonius [32] used a high-order accurate shock- and interface-capturing scheme to investigate shock-induced collapses of pre-existing nuclei near a solid surface that result in lithotripter pulses. Sezal [33] analyzed the potential of a density-based compressible flow solver with a homogeneous mixture model (thermodynamic equilibrium) to capture the bubble collapse dynamics. The same numerical scheme as applied by [33] is utilized in the present study in the CFD code hydRUB. Schmidt et al. [34] showed that pressure wave propagation is independent of the spatial resolution and thus the maximum wall pressure, the impulse strength, and the collapse duration are nearly independent of the applied spatial resolution, if the collapse occurs in a certain distance to the wall.

In contrast to Lauer's work [14], we apply a homogeneous mixture model and assume the liquid and vapor phase to be at thermodynamic equilibrium similar to [33]. We assume initially spherical single bubbles at their maximum size, which then collapse in response to the high constant ambient pressure. We neglect the fact that bubbles may occur in clouds and interact [35], which enhances the pressure load due to the interaction of emitted shock waves with neighboring bubbles as well as the occurrence of nonspherical vapor bubbles. It is known that the formation of the re-entrant jet and the resultant pressures are highly dependent on the initial wall standoff distance L_0/R_0 [31,36]. It has been found that the wall pressure load can be expressed as a function of the nondimensional radius r/R_0 and is the same for equal nondimensional initial standoff distances [31,32,36,37]. In the present study, we varied this nondimensional standoff distance in order to obtain different "pressure load profiles" – the maximum wall pressure with respect to the time at the wall.

Please cite this article as: F. Pöhl, et al., Evaluation of cavitation-induced pressure loads applied to material surfaces by finite-element-assisted pit analysis and numerical investigation of the..., Wear (2015), http://dx.doi.org/10.1016/j.wear.2014.12.048

We study numerically the effect of single spherical bubble collapses near the wall using a compressible density-based flow algorithm with an explicit time integration scheme. The convective fluxes are modeled with a Godunov-type flux formulation that is consistent for low Mach-numbers [38] and accounts for pressure wave propagation in liquids with low compressibility. Since the driving effects behind cavitation erosion are inertia-driven [39], we neglect viscous effects as well as turbulent effects. We assume a homogeneous mixture of liquid and vapor, so that both phases are in thermodynamic equilibrium and phase change follows an isentropic path [40]. Hence, the density is only dependent on the pressure, which has been realized by a barotropic equation of state (EOS). Because of the large pressure range – from the saturation pressure inside the bubble up to the high-pressure peaks at bubble collapse – we are obliged to deal with two different barotropic EOSs. Between the pressure range from 600 Pa to 300 MPa we use the highly accurate IAPWS-95 formulation (valid up to 1000 MPa) [41]. For the higher pressure range $p \geq 300$ MPa, we use the Thompson representation of the Tait equation [42], which is valid up to 2500 MPa (Eq. (4)). We assume its validity up to the highest occurring pressures of ~100,000 MPa.

$$p = p(\rho) = B\left[\left(\frac{\rho}{\rho_0}\right)^n - 1\right] + p_0 \quad \text{for} \quad p \geq 300 \text{ MPa} \tag{4}$$

Table 1
Maximum pressure inside the domain and collapse time for three different grid resolutions.

Grid resolution, R_0	25 cells	50 cells	100 cells
p_{max} (MPa)	779	2293	5940
$t_{collapse}$ (ns)	35.870	35.899	35.941

The constants for water are defined as $B = 3.31 \times 10^8$ Pa, $n = 7.15$, and $\rho_0 = 998.2$ kg/m^3. For a detailed description of the numerical algorithm, refer to previous publications [43,44].

2.6.1. Grid study and validation

Following Lauer et al. [14] and Sezal [33], we performed a grid study for the simulation of a 3D spherical vapor bubble collapse in water in order to evaluate the grid dependency of the results. For this purpose, we simulated the bubble collapse on three successively refined grids with 25, 50, and 100 cells per initial bubble radius R_0.

All three grid resolutions predict the same collapse dynamics (changing rate of the radius and the collapse time), whereas the maximum collapse pressure (p_{max}) at the bubble center is highly grid dependent and increases directly with the grid resolution (Table 1). The pressure at the bubble center is indeed highly grid-dependent, but the value of interest – the wall pressure – is assumed to be grid-independent [34]. Thus, we decided to follow the approach of Lauer [14], which resolves the initial bubble radius R_0 with 100 cells and dimensions the outer domain by 25 times the initial radius.

In the computations we investigated single bubble collapse in vicinity of the walls without considering the wall deformation (rigid wall). In order to validate our model for predicting of the wall pressure load profile, we compared the collapsing behavior and jet formation as well as the maximum wall pressures with respect to time against numerical results from Lauer [14]. We reproduced the numerical setup of Lauer (Fig. 6a) and simulated four different initial standoff distances: $L_0/R_0 = -0.35, 0, 0.35, 1.04$ (case *C*, *X*, *B*, *A*; cf. Fig. 6b). The initial fluid properties are defined on the basis of the barotropic EOS for an ambient liquid pressure of 100 bar and for a vapor volume fraction $\alpha = 0.99$ inside the bubble (Table 2).

We can qualitatively reproduce the collapse evolution and jet formations from Lauer, e.g. for the bubble configuration $L_0/R_0 = 0.35$: a re-entrant jet forms in the direction of the wall,

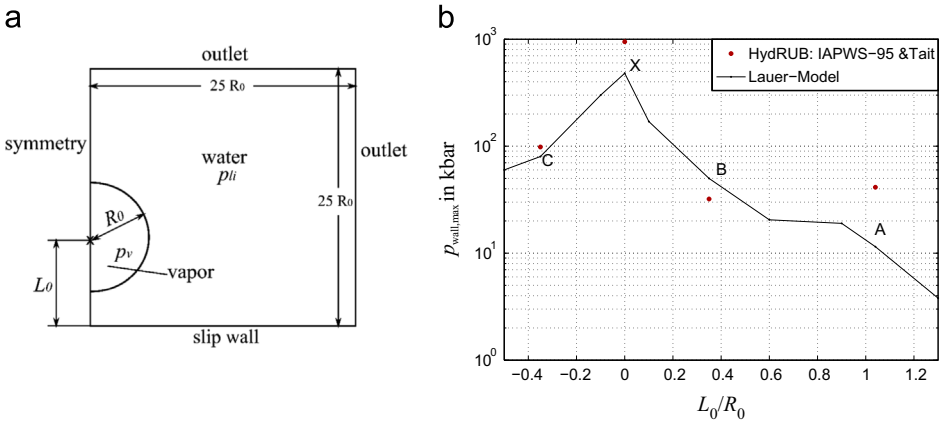

Fig. 6. (a) Sketch of the numerical setup of a near-wall bubble collapse for different wall standoff distances (*C*, *X*, *B*, *A*), and (b) maximal pressure load at the wall for different initial wall standoff distances L_0/R_0 compared to results of Lauer [14].

Table 2
Initial conditions for the vapor volume fraction α, pressure p and density ρ for the validation test case and for the parameter study.

Initial conditions	Validation test case		Parameter study	
	Vapor water	Liquid water	Vapor water	Liquid water
α	0.99	0	0.99	0
p (Pa)	$p_v = p_{baro}(\alpha) = 2185.2$	$p_{li} = 100 \times 10^5$	$p_v = p_{baro}(\alpha) = 2185.2$	$p_{li} = 100 \times 10^5$
ρ(kg/m^3)	$\rho_{baro}(\alpha) = 9.992$	$\rho_{baro}(\alpha_{li}) = 1026.6$	$\rho_{baro}(\alpha) = 9.992$	$\rho_{baro}(\alpha_{li}) = 1026.6$

Please cite this article as: F. Pöhl, et al., Evaluation of cavitation-induced pressure loads applied to material surfaces by finite-element-assisted pit analysis and numerical investigation of the..., Wear (2015), http://dx.doi.org/10.1016/j.wear.2014.12.048

generating a water-hammer shock and leading to a second wall-parallel outward-pointing jet that interacts with the remaining vapor bubble ring and leads to a secondary collapse [14].

By comparing the maximum wall pressure with that of Lauer (Fig. 6 b), we can predict the qualitative trend of the maximum wall pressure, which is dependent on the initial standoff distance L_0/R_0, although we slightly overestimate the wall pressure [14]. We conclude that, in spite of its simplifications (homogenous mixture model in thermodynamic equilibrium, neglecting surface tension), our model can capture the collapse evolution and jet formation of bubbles in the vicinity of the wall and is able to predict the wall pressure load profiles.

2.6.2. Parameter study

We set up a parameter study with a variable initial standoff distance. The setup and grid resolution is the same as for the validation test case (see Fig. 6(a) and Table 2). The single bubble simulations have been performed under typical ultrasonic horn conditions, assuming an ambient pressure of 1 bar and initial bubble radii between 10 and 120 µm which have been drawn from measured bubble spectra [45]. As noted in Section 2.6, the initial bubble radius R_0 has no effect on the distribution of p_{max} vs. r/R_0, so that any initial radius R_0 can be chosen for the simulation. The following wall distances were simulated: $L_0/R_0 = -0.5$, 0.0, 0.1, 0.2, 0.3, 0.4, 0.5, 1.0.

We assume that a pit forms on the material surface when the wall pressure is large enough to result in high equivalent stresses that exceed the local material yield stress (σ_y) [46]. Based on this assumption, we derived a scaling procedure to reconstruct a representative initial bubble radius R_B, which is sketched in Fig. 7. We only account for wall pressure load profiles exceeding the local yield stress σ_y, which is defined for each pit by its pit depth (see Fig. 5). In a first step, we calculated the intersection of the yield stress line with the pressure load profiles (CFD and FEM), which gave two length values: $a_{CFD}/R_{0,CFD}$ (nondimensional) and a_{FEM} (dimensioned) (Fig. 7). In a second step, we used the ratio equation:

$$R_B = a_{FEM}\left(\frac{a_{CFD}}{R_{0,CFD}}\right)^{-1} \quad (5)$$

to calculate a representative initial bubble radius R_B for each wall pressure load profile exceeding the yield stress. If the wall pressure load profile (CFD) – starting from the intersection point (with σ_y) – has a similar course as the assumed pit load profile (FEM), we assumed that configuration (L_0/R_0, and R_B) to be a possible scenario that, leads to the measured pit.

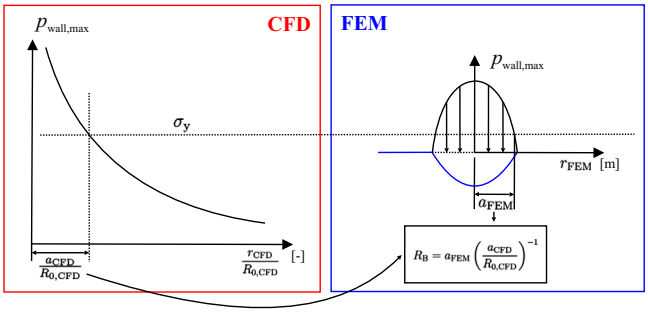

Fig. 7. Sketch of the dimensioning procedure to recalculate possible bubble/-wall configurations from pressure wall load profiles (CFD) and pit load profiles (FEM). b_{FEM} is a dimensioned parameter that results from FEM-load profiles of the measured pits.

3. Results and discussion

Fig. 8(a) shows the mean load–displacement curves of the copper specimen measured with the Berkovich and cube corner indenters. Fig. 8(b) shows the hardness as a function of the indentation depth. The hardness (strength) of the material increases with decreasing indentation depth. This is caused by the mechanical sample preparation and is superimposed by the ISE. The measured load–displacement curves were used to determine the depth-dependent material parameters given in Fig. 5 using an inverse procedure described in [19]. These parameters were used as input data for the numerical simulations within the algorithm used to calculate the pressure induced by collapsing bubbles. Though, it is known that there are differences between the interaction with the material surface of a bubble reentrant liquid jet and the solid fixed shape of an indenter [47]. Cavitation pressure load results in high stress waves in the material and a complex time history of pressure on the wall [46]. In contrast, indentation load leads to a continuous contact pressure and to material deformation with a low strain rate. Thus, the numerically calculated deformation (using the material properties derived by indentation) can deviate from the deformation behavior under cavitation load.

Figs. 9 and 10, respectively, show the surface of the copper sample before and after exposure to cavitation. After exposure to

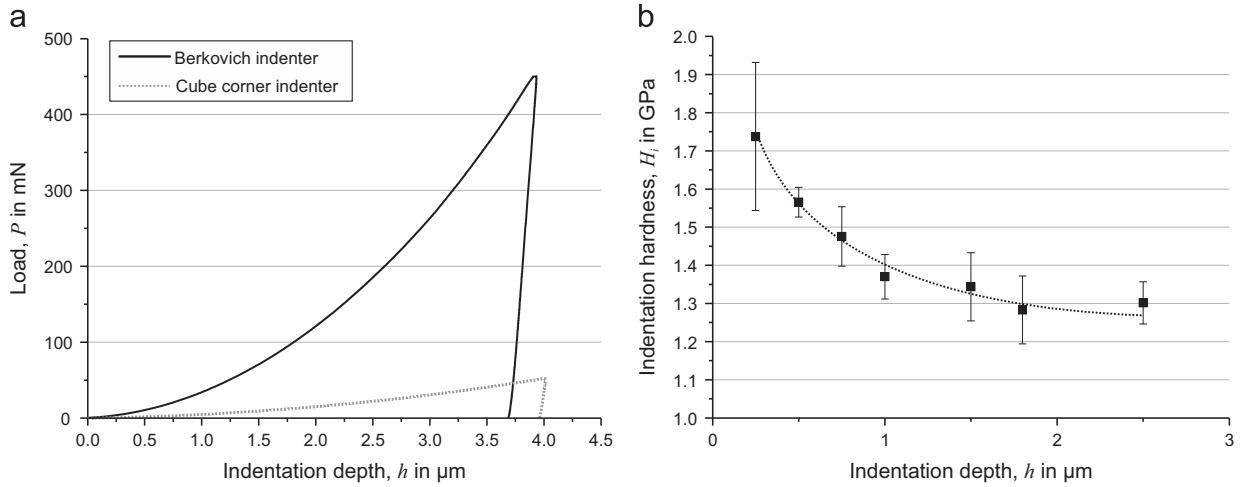

Fig. 8. Results of instrumented indentation tests on copper: (a) Mean load–displacement curves. (b) Hardness as a function of the indentation depth (Berkovich indenter).

Please cite this article as: F. Pöhl, et al., Evaluation of cavitation-induced pressure loads applied to material surfaces by finite-element-assisted pit analysis and numerical investigation of the..., Wear (2015), http://dx.doi.org/10.1016/j.wear.2014.12.048

cavitation, isolated and already overlapping pits were found. The geometries of only single, non-overlapping pits were taken into account in the analysis. Fig. 11(a) shows a typical pit with a nearly axially symmetric geometry, which can be approximated by a 2D height profile, as given in the figure.

Fig. 11(a) shows the measured height profile as well as the numerically calculated profile after optimization. The calculated pressure distribution on the surface is illustrated in Fig. 11(b). The results of all analyzed pits are presented in Fig. 12. The calculated maximum pressures p_{max} are in the range between approx. 2400 MPa and 3500 MPa. Fig. 12 shows that there is a relationship between the maximum pressure and the ratio between pit the width and the pit depth (b/h). The higher the b/h ratio, the lower is the maximum pressure that is necessary to form the pit. Broad pits with a low depth were caused by pressure fields with low maximum pressures, in contrast to narrow pits with a high depth that are caused by higher maximum pressures.

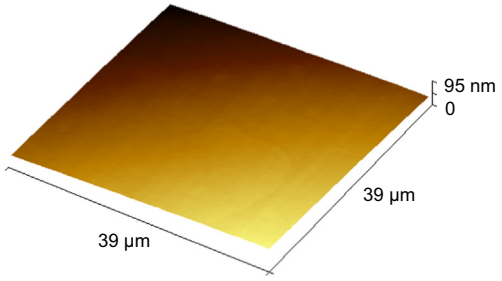

Fig. 9. AFM topography of the copper sample before exposure to cavitation.

The known pressure distribution on the surface and the given material behavior were used for the numerical calculation of the elasto-plastic deformation of copper under the cavitation-induced pressure load. The deformation behavior of all investigated pits is very similar and exemplarily presented for one analyzed pit in Fig. 13. The diagram shows the equivalent plastic strain distribution ε_{pl} in the material caused by the applied stress distribution of Fig. 11(b). The applied load leads to a maximum plastic strain in a subsurface region that is very similar to a Hertz-like contact between a rigid sphere and an elastic half-space [48]. The maximum strain is located below the surface at a depth of approximately one eight of the pit diameter, whereas the maximum strain

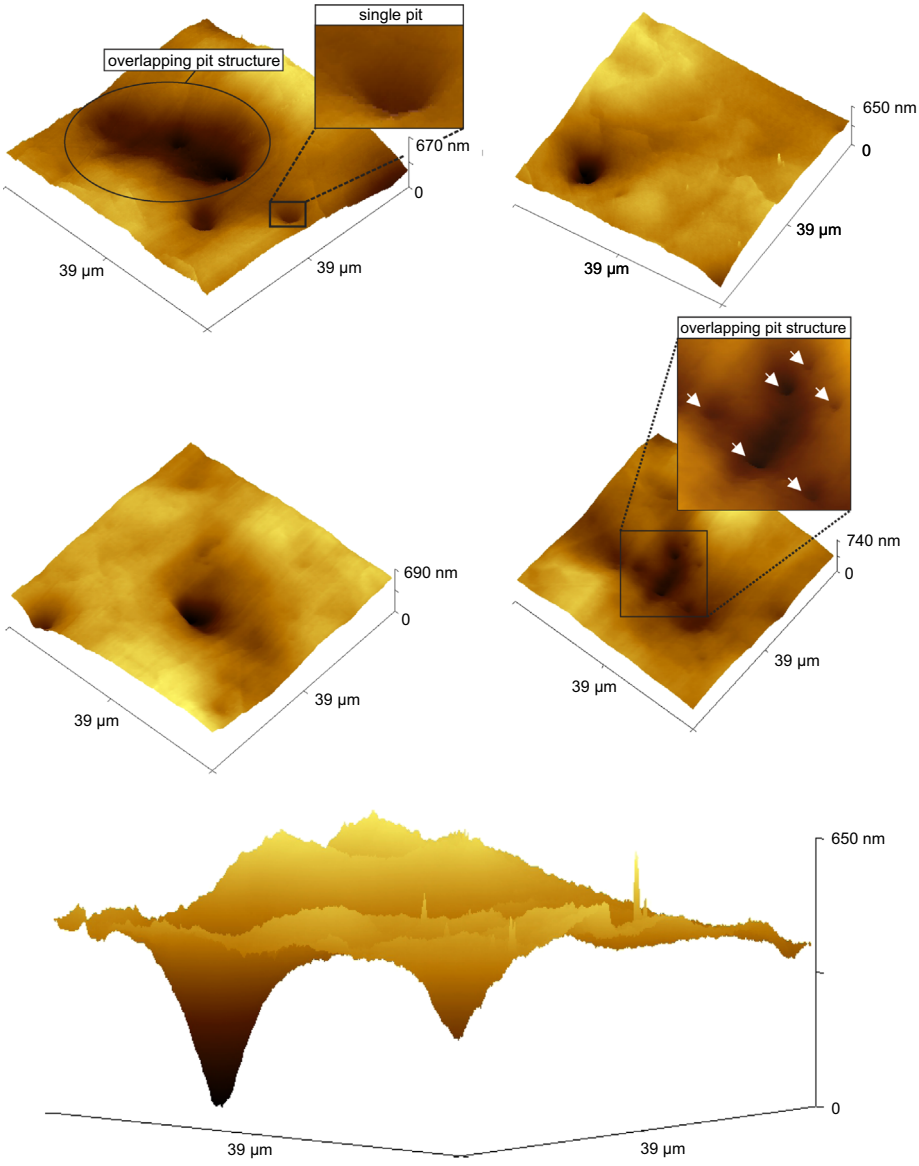

Fig. 10. AFM topography of the copper sample after exposure to cavitation.

Please cite this article as: F. Pöhl, et al., Evaluation of cavitation-induced pressure loads applied to material surfaces by finite-element-assisted pit analysis and numerical investigation of the..., Wear (2015), http://dx.doi.org/10.1016/j.wear.2014.12.048

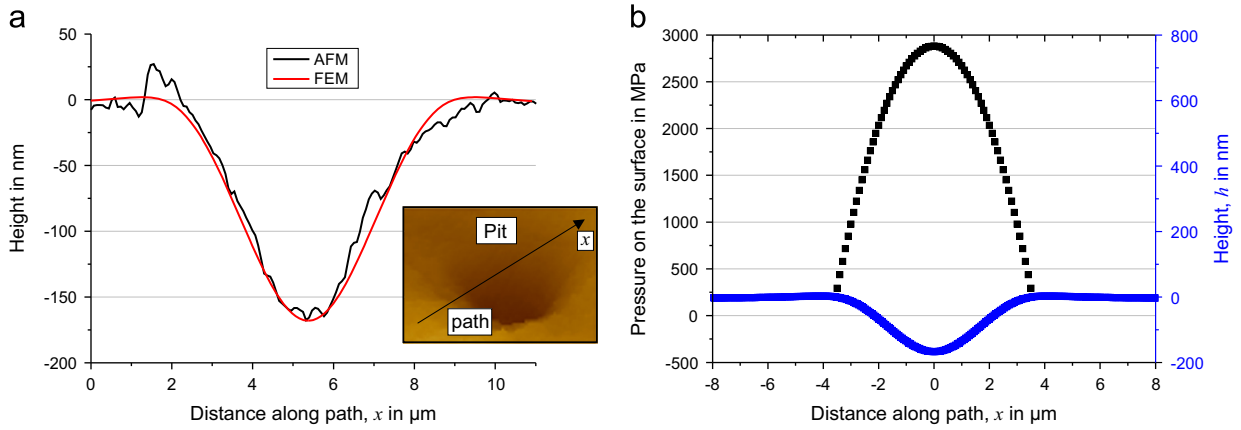

Fig. 11. (a) Topography of a nearly axis-symmetric pit: representative height profile(AFM) and numerically determined height profile after optimization (FEM). (b) Numerically calculated pressure distribution on the surface and height profile of pit.

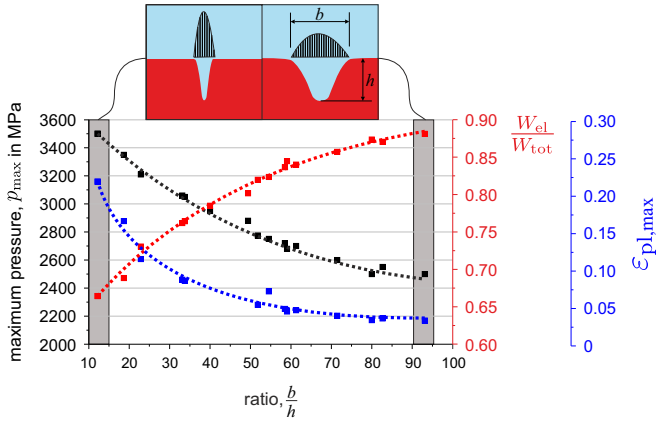

Fig. 12. Relationship between maximum pressure p_{max}, ratio of elastic to total deformation energy W_{el}/W_{tot}, maximum plastic strain $\varepsilon_{pl,max}$, and the ratio of pit width to pit depth b/h.

of a Hertz-like contact is approximately located below the surface at a depth of one fourth of the contact diameter [48]. Fig. 12 reveals that the maximum plastic strain is similar to the maximum pressure dependent on the ratio between the pit width and the pit depth. Narrow pits with a high depth obey the highest maximum plastic strains. The maximum of stress and strain in a subsurface region indicates that damage and fatigue cracks might occur and propagate preferably from these regions. Furthermore, the energy necessary for elasto-plastic deformation (strain energy) was analyzed. Fig. 14 illustrates the total energy expenditure for elasto-plastic deformation (forming the pit). Since the FEM simulations are static calculations the time axis in Fig. 14 has no physical meaning. During loading the total energy increases to a maximum, whereas during unloading a high ratio of energy is elastically released due to elastic recovery. The ratio of elastic to total deformation energy W_{el}/W_{tot} is found to be in the range between approx. 66 and 88%. The high ratio of elastic strain energy explains the sink-in behavior of the material around the measured pits (see Fig. 16). Due to the high ratio of elastic deformation, the material around the pit is compressed and pushed downwards. This behavior is well known from indentation imprints and is favored by elastic deformation [49]. All investigated pits show the described sink-in behavior.

The W_{el}/W_{tot} ratio also depends on the pit geometry. The higher the ratio of pit width to pit depth, the higher is W_{el}/W_{tot}. This is inversely proportional to the maximum pressure p_{max} and maximum plastic strain $\varepsilon_{pl,max}$ (see Fig. 12). Narrow pits with high depths are formed by a high maximum pressure. This leads to higher plastic deformation in the material and consequently at the same time to a reduction in the W_{el}/W_{tot} ratio. Conversely, broad pits with low depths are caused by lower maximum pressures leading to lower plastic deformation and higher W_{el}/W_{tot} ratios. The relationships between pit geometry and the calculated parameter p_{max}, $\varepsilon_{pl,max}$ and W_{el}/W_{tot} are summarized in Fig. 15.

In the FEM simulations the pressure load caused by collapsing bubbles was assumed to be static (time independent). Though, it is known from bubble/material interaction modeling [47] and from cavitation flow field measurements [47,50] that impulsive loading from cavitation is highly unsteady and dependent on both time and space. These effects are not taken into account in the FEM model and the calculated pressure profiles are idealized loads simplifying the complex time history on the wall. Furthermore, the material properties derived by indentation do not account for the highly dynamic time-dependent material behavior.

In order to assess the influence of the simplifying assumptions made in the inverse algorithm (stationary bell-shape pressure profile, neglecting possible influences of temperature as well as high deformation speed), CFD simulations of near-wall vapor bubble collapses have been performed to determine the wall pressure load profiles. The maximum pressure over time is considered at each spatial location of the profile.

The wall pressure load profiles versus the nondimensional radius r/R_0 are shown in Fig. 17. The reconstructed initial bubble Radii R_B are given in Table 3. The following observations can be ascertained from the parameter study:

- We assume that uncut bubble configurations ($L_0/R_0 > 1$) do not exceed the yield stress limit (cf. Fig. 3, $L_0/R_0 = 1$). We observe that – expect the cases $L_0/R_0 < 0$ – the maximum wall pressure occurs in a certain distance to the collapse center, where the overall maximum pressure occurs. Therefore, we assume that the maximum wall pressure is – in contrast to the overall maximum pressure – essentially grid independent according to [34].
- Bubbles, which are cut below the center (cf. Fig. 3, $0 < L_0/R_0 < 1$), lead to local maximum pressures at a distance from the bubble centerline. This behavior results from the second wall-parallel outward-pointing jet interacting with the remaining vapor bubble ring. We find this behavior also described by Lauer et al. [14] and Johnsen and Colonius [32].
- Most of the reconstructed bubble radii R_B are in the expected order of magnitude, in the range between 10 and 120 µm (Table 3) [45], while some bigger bubbles were reconstructed.

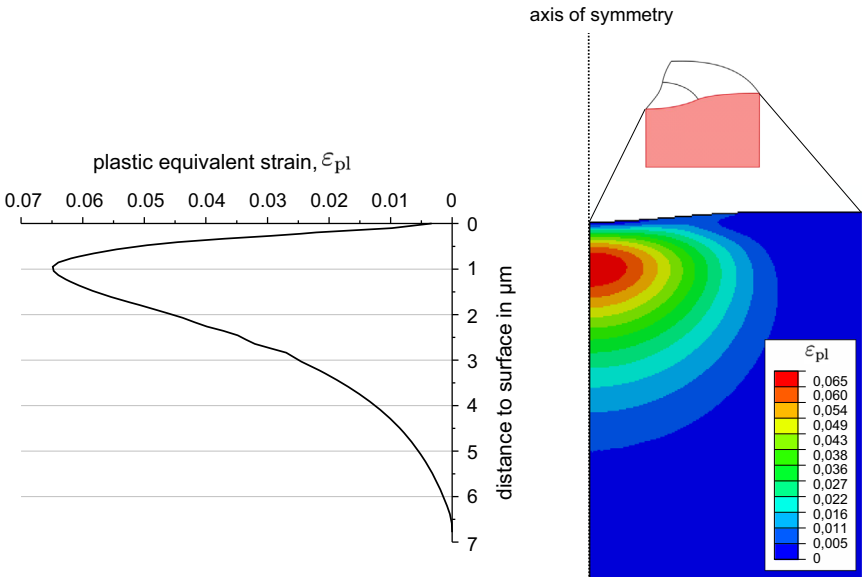

Fig. 13. Calculated plastic strain distribution of a measured pit in copper with the profile of plastic strain along the axis of symmetry.

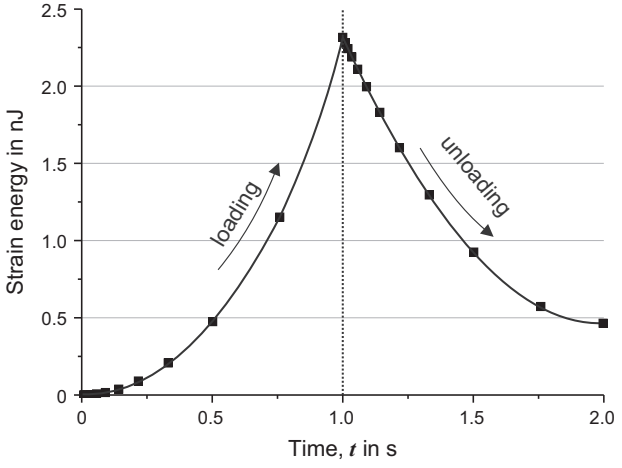

Fig. 14. Strain energy of elastic and plastic deformation during loading and unloading.

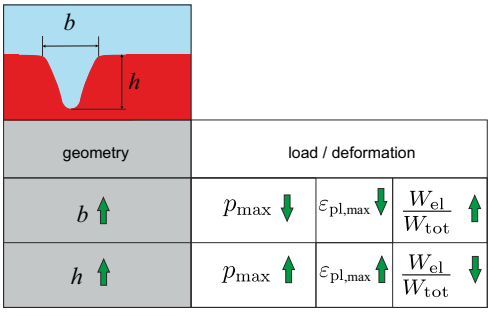

Fig. 15. Summary of the relationships between the pit geometry (b and h) and the maximum pressure p_{max}, the ratio of elastic to total deformation energy W_{el}/W_{tot}, and the maximum plastic strain $\varepsilon_{pl,max}$.

We attribute this observation to the fact, that in [45] bubbles in a certain distance to the wall were recorded and that, bubbles in immediate vicinity of the wall may have non-spherical shape.

- Small and deep pits result from smaller initial bubbles, whereas wider and flatter pits result from bigger initial radii (Table 3).

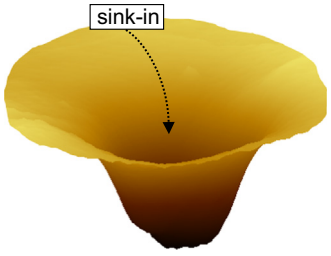

Fig. 16. AFM image of a pit in copper with sink-in behavior of the surface around the pit.

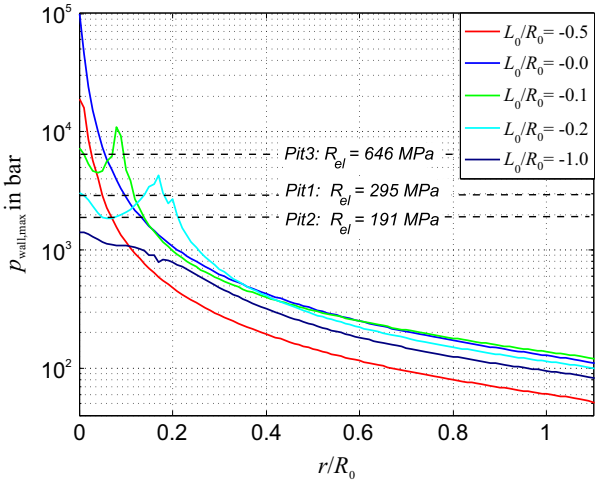

Fig. 17. Wall pressure load profiles for different nondimensional initial wall standoff distances and local yield stress lines for three different measured pits: pit1: width/depth=38.2; pit2: width/depth=57.7 and pit3: width/depth=84.2.

- We could not directly assign a wall pressure load profile to a measured pit. The assumed FEM load profiles differ from the wall load profiles (CFD) as they are found to be wider.
- We classify three types of wall load profiles for cut bubble configurations (Fig. 17):
  1. Bubbles cut above their center ($-1 < L_0/R_0 < 0$) lead to sharp wall load profiles.

Table 3
Reconstructed initial bubble radii R_B for three measured pits with different width/depth ratios. Only the initial standoff distances $L_0/R_0 = -0.5$, 0, 0.1 are taken into account.

Pit no.	Local σ_y (MPa)	b/h (–)	L_0/R_0 (–)	R_B (μm)	Sketch
1	295	32.2	−0.5	124.3	
			0	63.5	
			0.1	52.4	
2	191	57.7	−0.5	210.1	
			0	110.2	
			0.1	104.9	
3	646	84.2	−0.5	250.2	
			0	123.2	
			0.1	701	

2. Bubbles cut directly at their center ($L_0/R_0 = 0$) lead to nearly exponentially increasing wall loads in the direction of the centerline. We have to consider that the peak pressure directly at the centerline is highly grid-dependent due to the fact that the wall itself represents the collapse center where the waves propagate forward.
3. Bubbles cut below their center ($0 < L_0/R_0 < 1$) lead to wall load profiles with local maximum pressures at a distance from the centerline.

4. Conclusions

This paper presents a method for calculating the cavitation-induced pressure loads on material surfaces based on the analysis of single cavitation pits and CFD simulations. The results create a link between the cavitation load and material deformation. In combination with FEM simulations, they provide an insight into the deformation behavior of copper under cavitation loading. We also propose a numerical approach based on CFD for reconstructing possible bubble wall collapse configurations (L_0/R_0, and R_B) from measured pit loads, assuming spherical single bubbles. We have verified that our compressible CFD model is able to predict the collapse evolution and jet formation of spherical bubble collapses in the vicinity of the wall and have conducted a parameter study with variation of initial standoff distance L_0/R_0. The following conclusions can be drawn:

- The isolated cavitation pits found on the copper sample are nearly axially symmetric, indicating that the pressure distribution applied to the material surface by collapsing bubbles is also axially symmetric.
- The calculated (inverse algorithm) maximum pressures p_{max} from the measured pit geometry induced by single collapsing bubbles in the ultrasonic vibratory apparatus are between 2400 MPa and 3500 MPa.
- FEM simulations of copper show that the maximum stresses and strains caused by the calculated pressures occur in a subsurface region at a depth of approximately one eighth of the pit diameter. Damage and fatigue cracks might occur at first and start at these positions. The deformation is very similar to a Hertz-like contact between a rigid sphere and an elastic half-space [48]. The maximum plastic strains were calculated to be 4–23%.
- The calculated deformation of copper shows a high elastic ratio. Approx. 66–87% of the deformation energy is elastic and is released during unloading. The high ratio of elastic deformation explains the observed sink-in of the material around the cavitation pits.
- The maximum pressure, the maximum plastic strain, and the ratio of elastic to total deformation energy correlate well with the ratio between pit width and pit depth. Narrow pits with high depths are formed by a high maximum pressure, which leads to higher plastic deformation in the material and consequently at the same time to a reduction of the W_{el}/W_{tot} ratio. Conversely, broad pits with low depths are caused by lower maximum pressures leading to lower plastic deformation and higher W_{el}/W_{tot} ratios.
- The validation of the density-based flow algorithm shows that our compressible CFD model is able to predict the collapse evolution and jet formation of spherical bubble collapses in the vicinity of the wall.
- It is concluded that we are able to capture the trend in which small and deep pits result from smaller initial bubbles, whereas wider and flatter pits result from bigger bubbles. Currently, we are not able to assign an exact wall collapse configuration ($L_0/R0$, and R_B) to a measured pit shape. We assume that we need an additional parameter that differs the FEM load profiles in two classes: with and without local maximum pressure at a distance from the centerline.

An improved pressure load profile and transient effects will be considered in the FEM algorithm in further research of the authors.

Acknowledgments

The authors gratefully acknowledge financial support by the Kompetenzzentrum Hydraulische Strömungsmaschinen at the Ruhr-Universität Bochum (Germany).

References

[1] S. Hattori, T. Hirose, K. Sugiyama, Wear 269 (2010) 507–514.
[2] M.-K. Lee, S. Hong, G. Kim, K. Kim, C. Rhee, W. Kim, Mater. Sci. Eng. A 425 (2006) 15–21.
[3] M. Pohl, J. Stella, C. Hessing, Adv. Eng. Mater. 5 (2003) 251–256.
[4] J. Stella, M. Pohl, C. Bock, U. Kunze, Wear 316 (2014) 1–5.
[5] P. Niederhofer, S. Huth, Wear 301 (2013) 457–466.
[6] S. Brunatto, A. Allenstein, C. Allenstein, A. Bushinelli, Wear 247–245 (2012) 220–228.
[7] H. Chen, W. Wu, Mater. Sci. Eng. A 489 (2008) 451–456.
[8] M. Pohl, J. Stella, Wear 252 (2002) 501–511.
[9] B. Rao, D. Buckley, Mater. Sci. Eng. 67 (1984) 55–67.
[10] A. Karimi, Mater. Sci. Eng. 86 (1987) 191–203.
[11] T. Okada, Y. Iwai, S. Hattori, N. Tanimura, Wear 184 (1995) 231–239.
[12] I. Tzanakis, D. Eskin, A. Georgoulas, D. Fytanidis, Ultrason. Sonochem. 21 (2014) 866–878.
[13] D. Carnelli, A. Karimi, J. Franc, Wear 289 (2012) 104–111.
[14] E. Lauer, X. Hu, S. Hickel, N. Adams, Comput. Fluids 69 (2012) 1–19.
[15] ASTM G32-10, Test Method for Cavitation Erosion using Vibratory Apparatus (2010).
[16] M. Dular, B. Stoffel, B. Sirok, Wear 261 (2006) 642–655.
[17] M. Ashokkumar, Ultrason. Sonochem. 18 (2011) 864–872.
[18] S. Merouani, O. Hamdaoui, V. Rezgui, M. Guemini, Ultrason. Sonochem. 21 (2014) 53–59.
[19] F. Pöhl, Randschichtbeanspruchung metallischer Werkstoffe durch Indentation and Kavitation (Ph.D. thesis), Ruhr-Universität Bochum, 2014.
[20] F. Pöhl, S. Huth, W. Theisen, J. Mech. Phys. Solids 66 (2014) 32–41.
[21] W. Oliver, G. Pharr, J. Mater. Res. 7 (1992) 1564–1583.
[22] W. Oliver, G. Pharr, J. Mater. Res. 19 (2004) 3–20.
[23] G. Pharr, E. Herbert, Y. Gao, Annu. Rev. Mater. Res. 40 (2010) 271–290.
[24] W. Nix, H. Gao, J. Mech. Phys. Solids 46 (1998) 411–425.
[25] Y. Huang, F. Zhang, K. Hwang, W. Nix, G. Pharr, G. Feng, J. Mech. Phys. Solids 54 (2006) 1668–1686.
[26] Y. Liu, A. Ngan, Depth dependence of hardness in copper single crystals measured by nanoindentation, Scr. Mater. 44 (2001) 237–241.
[27] J. Nelder, R. Mead, Comput. J. 7 (1965) 308–313.
[28] F. Pöhl, S. Huth, W. Theisen, Mater. Sci. Eng. A 559 (2013) 822–828.

Please cite this article as: F. Pöhl, et al., Evaluation of cavitation-induced pressure loads applied to material surfaces by finite-element-assisted pit analysis and numerical investigation of the..., Wear (2015), http://dx.doi.org/10.1016/j.wear.2014.12.048

[29] M. Dao, N. Chollacoop, K. VanVliet, T. Venkatesh, S. Suresh, Acta Mater. 49 (2001) 3899–3918.
[30] Rayleigh, Philos. Mag. 6 (1917).
[31] R. Chapman, M. Plesset, J. Basic Eng. 94 (1972).
[32] E. Johnsen, T. Colonius, J. Acoust. Soc. Am. 124 (2008).
[33] I. Sezal, Compressible dynamics of cavitating 3-D multi-phase flows (Ph.D. thesis), Technische Universität München, 2012.
[34] S. Schmidt, M. Mihatsch, M. Thalhamer, N. Adams, in: 3rd International Cavitation Forum (WIMRC), 2011.
[35] C.E. Brennen, Cavitation and Bubble Dynamics, Oxford University Press, Oxford, England, 1995.
[36] J. Blake, D. Gibson, Ann. Rev. Fluid Mech. 19 (1987).
[37] W. Lauterborn, H. Bolle, J. Fluid Mech. 72 (1975).
[38] G. Schnerr, I. Sezal, S. Schmidt, Phys. Fluids 20 (2008).
[39] J. Franc, J. Michel, Fundamentals of Cavitation, Springer-Verlag, Berlin, Germany, 2004.
[40] U. Iben, Sys. Anal. Mod. Sim. 42 (2002).
[41] W. Wagner, H.-J. Kretzschmar, International Steam Tables, Springer-Verlag, Berlin, Germany, 2008.
[42] P. Thompson, Compressible Fluid Dynamics, McGraw-Hill, New York, United States of America, 1972.
[43] C. Deimel, S. Mottyll, R. Skoda, M. Kiermeir, M. Günther, R. Schilling, in: Eighth International Conference on Computational Fluid Dynamics, (ICCFD8), 2014.
[44] S. Mottyll, S. Müller, P. Niederhofer, J. Hussong, S. Huth, R. Skoda, Exp. Fluid Mech. (EFM) 67 (2013) 1–9.
[45] S. Müller, M. Fischper, S. Mottyll, R. Skoda, J. Hussong, in: International Conference on Experimental Fluid Mechanics (EFM), 2013.
[46] C. Hsiao, A. Jayaprakash, A. Kapahi, J. Choi, G. Chahine, J. Fluid Mech. 755 (2014) 142–175.
[47] K. Kim, G. Chahine, J. Franc, A.E. Karimi, Advanced Experimental and Numerical Techniques for Cavitation Erosion Prediction: Series Fluid Mechanics and its Applications, vol. 106, Springer, Berlin, 2014.
[48] H. Hertz, J. Angew. Math. 92 (1881) 156–171.
[49] B. Taljat, G. Pharr, Int. J. Solids Struct. 41 (2004) 3891–3904.
[50] S. Singh, J. Choi, G. Chahine, ASME J. Fluids Eng. 135 (2013) 091302-1–091302-11.

Please cite this article as: F. Pöhl, et al., Evaluation of cavitation-induced pressure loads applied to material surfaces by finite-element-assisted pit analysis and numerical investigation of the..., Wear (2015), http://dx.doi.org/10.1016/j.wear.2014.12.048